Electronic structures and multi-orbital models of $La_3Ni_2O_7$ thin films at ambient pressure

Xunwu Hu[1,2†], Wenyuan Qiu[2†], Cui-Qun Chen[2], Zhihui Luo[2], Dao-Xin Yao[2*]

[1]Department of Physics, College of Physics and Optoelectronic Engineering, Jinan University, Guangzhou, 510632, China.
[2]Center for Neutron Science and Technology, Guangdong Provincial Key Laboratory of Magnetoelectric Physics and Devices, State Key Laboratory of Optoelectronic Materials and Technologies, School of Physics, Sun Yat-Sen University, Guangzhou, 510275, China.

*Corresponding author(s). E-mail(s): yaodaox@mail.sysu.edu.cn;
†These authors contributed equally to this work.

Abstract

The recent discovery of superconductivity with a transition temperature $\boldsymbol{T_c}$ exceeding 40 K in $\mathbf{La_3Ni_2O_7}$ and $\mathbf{(La,Pr)_3Ni_2O_7}$ thin films at ambient pressure marks a significant breakthrough in the field of nickelate superconductors. Using density functional theory (DFT), we propose a double-stacked two-orbital effective model for $\mathbf{La_3Ni_2O_7}$ thin film based on the Ni$-\boldsymbol{e_g}$ orbitals. Our analysis of the Fermi surface reveals three electron pockets ($\boldsymbol{\alpha, \alpha', \beta}$) and two hole pockets ($\boldsymbol{\gamma, \gamma'}$), where the additional $\boldsymbol{\alpha'}$ and $\boldsymbol{\gamma'}$ pockets arise from inter-stack interactions. Furthermore, we introduce a high-energy model that incorporates O$-\boldsymbol{p}$ orbitals to facilitate future studies. Calculations of spin susceptibility within the random phase approximation (RPA) indicate that magnetic correlations are enhanced by nesting of the $\boldsymbol{\gamma}$ pocket, which is predominantly derived from the Ni$-\boldsymbol{d_{z^2}}$ orbital. Our results provide a theoretical foundation for understanding the electronic and magnetic properties of $\mathbf{La_3Ni_2O_7}$ thin films.

1 Introduction

The discovery of superconductivity in the Ruddlesden-Popper (RP) bilayer nickelate $La_3Ni_2O_7$ at a transition temperature T_c near 80 K under high pressure ($\sim$ 14 Gpa) has generated significant interest in the field of unconventional superconductivity [1]. The subsequent observation of superconductivity in the trilayer nickelate $La_4Ni_3O_{10}$ under similar conditions further underscores the universality of superconductivity in nickelates [2]. These discoveries have motivated extensive theoretical [3–38] and experimental [39–47] investigations into the microscopic mechanisms of unconventional superconductivity. However, the requirement of high pressure for superconductivity in $La_3Ni_2O_7$ and $La_4Ni_3O_{10}$ presents significant experimental challenges, which limit in-depth investigations. This has driven efforts to stabilize superconductivity under ambient pressure, facilitating a more comprehensive understanding of its underlying mechanisms.

Recent studies have reported superconductivity with T_c exceeding 40 K in $La_3Ni_2O_7$ [48], $(La,Pr)_3Ni_2O_7$ [49, 50] thin films at ambient pressure, marking a significant breakthrough in nickelate superconductors. X-ray absorption spectroscopy (XAS) reveals that the Ni ions in $La_3Ni_2O_7$ thin film retain a mixed valence state similar to that of the bulk form [48]. Furthermore, scanning transmission electron microscopy (STEM) confirms that their microscopic structure closely resembles that of the bulk phase of high pressure, adopting a tetragonal crystal structure [49]. In particular, the T_c in the thin film is tunable via the in-plane lattice constant but remains relatively insensitive to the out-of-plane parameter. DFT calculation and angle-resolved photoemission spectroscopy (ARPES) measurement [51, 52] suggest that Ni-$d_{x^2-y^2}$ and Ni-d_{z^2} orbitals contribute states near the Fermi level, highlighting the similarity between the thin film and the bulk system in terms of electronic structure and superconducting properties. Despite these advances, most theoretical studies have relied on simplified half-unit-cell (Half-UC) slab model [53, 54], which may not fully capture the effects of dimensionality on the electronic structure. A more comprehensive approach incorporating the full-unit-cell slab model is therefore needed to provide a more accurate description of this system.

In this paper, we employ slab models of $La_3Ni_2O_7$ thin films to investigate their electronic structures in various thicknesses, including three-unit-cell (Three-UC), one-unit-cell (One-UC), and Half-UC configurations. Except for the Half-UC case, each slab model retains a complete unit cell (UC), with the two bilayers denoted as Stack 1 and Stack 2, enabling a systematic exploration of the relationship between dimensionality and electronic properties. Using first-principles calculations, we propose a double-stacked two-orbital effective model for the One-UC slab structure, based on Ni$-e_g$ orbitals. Our analysis reveals the presence of three electron pockets (α, α', β) and two hole pockets (γ, γ') on the Fermi surface, where inter-stack interactions give rise to the additional α' and γ' pockets. Furthermore, we extend our model by incorporating O$-p$ orbitals into a high-energy framework to facilitate future studies. Spin susceptibility calculations within the RPA indicate pronounced magnetic correlations, primarily driven by nesting effects of the γ pocket, which is predominantly derived from the Ni$-d_{z^2}$ orbital. Our results provide theoretical framework for understanding the

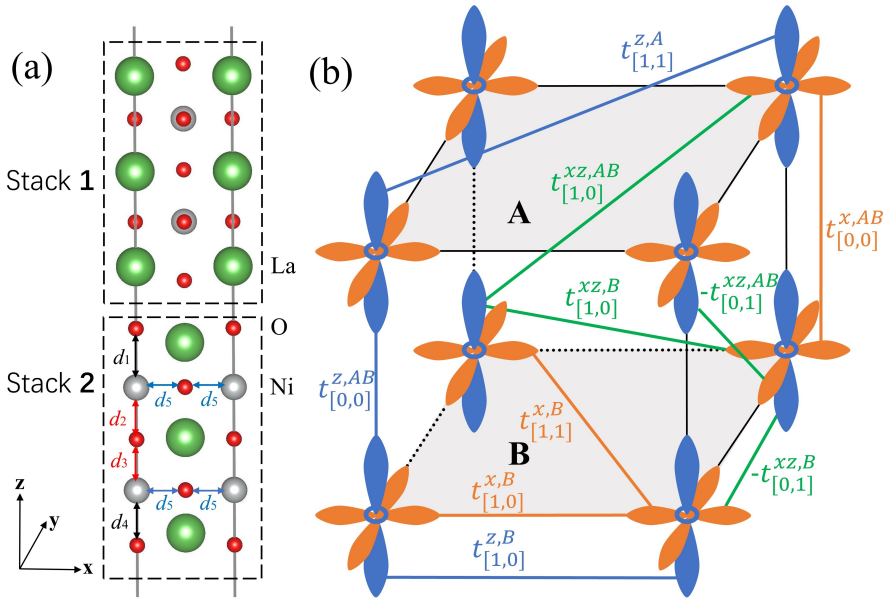

Figure 1 Slab structure and schematic illustration of the hopping parameters used in the $La_3Ni_2O_7$ thin-film model. (a) The free-standing One-UC slab structure of $La_3Ni_2O_7$, where the two bilayers are labeled as Stack 1 and Stack 2. Green, gray, and red spheres denote La, Ni, and O atoms, respectively. The outer-apical (d_1 and d_4), inner-apical (d_2 and d_3), and in-plane (d_5) Ni-O bond lengths are indicated by black, red, and blue arrows, respectively. (b) Schematic illustration of the hopping parameters in the $La_3Ni_2O_7$ thin films, highlighting the Ni$-d_{x^2-y^2}$ (orange) and d_{z^2} (blue) orbitals. Only nearest-neighbor hopping terms are shown.

interplay among the dimensionality, magnetism, and superconductivity in $La_3Ni_2O_7$ thin films, offering key insights for future theoretical and experimental investigations.

2 Results

2.1 Slab structures

We begin our investigation of the $La_3Ni_2O_7$ thin films by modeling the slab structures using DFT calculations. Bulk $La_3Ni_2O_7$ belongs to the $n = 2$ Ruddlesden-Popper phase, characterized by a UC comprising two corner-sharing NiO_6 octahedra bilayers stacking along the c axis [1]. In its thin-film form, $La_3Ni_2O_7$ adopts a tetragonal structure similar to the high-pressure bulk phase, distinguished by an apical Ni-O-Ni bond angle approaching 180° [48, 55]. To systematically explore the structural and electronic properties of $La_3Ni_2O_7$ thin films, we consider slab structures of varying thicknesses along the out-of-plane direction, including Three-UC, One-UC, and Half-UC slabs. To minimize interactions between preiodic images, a vacuum spacing exceeding 16 $\mathring{A}$ is introduced along the c axis.

The One-UC slab consists of two stacked NiO_6 octahedra bilayers, which can adopt two distinct stacking configurations, Stack 1 and Stack 2, as illustrated in Figure 1(a). In all slab models, we consider a free-standing geometry with a vacuum layer to

Table 1 The Ni-O bond lengths (d) in NiO_6 octahedra of $La_3Ni_2O_7$ slab structures under $U_{eff} = 0$ eV and $U_{eff} = 2$ eV. The unit of d are in $\mathring{A}$.

U_{eff} (eV)	Stack	d	Three-UC	One-UC	Half-UC
$U_{eff} = 0$	1	d_1	2.292	2.120	2.116
		d_2	1.965	1.973	2.003
		d_3	1.965	2.003	2.003
		d_4	2.282	2.276	2.116
		d_5	1.885	1.885	1.885
	2	d_1	2.282	2.276	–
		d_2	1.965	2.003	–
		d_3	1.965	1.973	–
		d_4	2.292	2.120	–
		d_5	1.885	1.885	–
$U_{eff} = 2$	1	d_1	2.308	2.133	2.120
		d_2	1.960	1.944	1.996
		d_3	1.960	2.012	1.996
		d_4	2.307	2.364	2.120
		d_5	1.885	1.885	1.885
	2	d_1	2.307	2.364	–
		d_2	1.960	2.012	–
		d_3	1.960	1.944	–
		d_4	2.308	2.133	–
		d_5	1.885	1.885	–

eliminate inter-slab interactions. The effect of epitaxial strain from the substrate is incorporated by fixing the in-plane lattice constant to the experimentally measured value of $a = 3.77\mathring{A}$ [48]. Although this approach does not capture all aspects of the experimental system—particularly in thicker films, where subtle differences between the top and bottom layers may occur—it provides a reasonable and reliable approximation for the few-layer systems considered in this study. The Ni-O bond lengths, labeled as d_1, d_2, d_3, d_4, and d_5 in Figure 1(a), are summarized in Table 1 for different slab structures and effective Hubbard parameters ($U_{eff} = 0$ eV and $U_{eff} = 2$ eV). For clarity, only the bond distances of the middle UC are reported for the Three-UC slab structure.

For $U_{eff} = 0$ eV, the in-plane Ni-O bond (d_5) is the shortest, while the outer-apical Ni-O bonds (d_1 and d_4) are the longest, consistent with the high-pressure phase of $La_3Ni_2O_7$. Different slab structures yield nearly identical results in terms of bond lengths. In the Three-UC and One-UC slabs, d_1 and d_4 vary across stacking configurations, while d_2 and d_3 also exhibit stack-dependent variations, indicating symmetry breaking between different stacks. The Ni-O bond lengths in these slabs follow a specific symmetry relation: in Stack 1, d_1, d_2, d_3, d_4 correspond to d_4, d_3, d_2, d_1 in Stack 2. In contrast, the Half-UC slab exhibits a distinct structural behavior, characterized by Ni-O bond lengths that are symmetric about the central oxygen atom, differing from the asymmetric distortions observed in the other slab structures. This difference arises from the underlying structural symmetry. In Half-UC, the slab posesses m_z symmetry, with the mirror plane located between the two NiO layers. This symmetry

enforces bond length equivalence with respect to the mirror plane, resulting in two nonequivalent vertical bond lengths. However, the One-UC and Three-UC slabs exhibit a different symmetry operation, $\{m_z|\frac{1}{2},\frac{1}{2},\frac{1}{2}\}$, where the mirror plane lies between two stacks. This symmetry allows for bond length variations within each individual stack, leading to distinct vertical bond lengths across the three stacks in the Three-UC slab, whereas only one stack exhibits such variations in the One-UC slab. This symmetry distinction is further reflected in the hopping parameters, influencing the electronic properties of the system.

For U_{eff} = 2 eV, electron correlation significantly influences the outer-apical Ni-O bond lengths (d_1 and d_4) in the Three-UC and One-UC slabs, whereas its effect is negligible in the Half-UC slab. Meanwhile, the in-plane Ni-O bond length (d_5) remains relatively stable in all configurations. These structural modifications are expected to have a pronounced impact on the electronic structures, which will be examined in detail in the following subsection. These findings highlight the critical role of interlayer interactions in determining the structural properties, which cannot be adequately captured by the Half-UC slab.

2.2 Electronic structures

We now investigate the electronic structures of $La_3Ni_2O_7$ thin films based on DFT calculations. For U_{eff} = 0 eV, the band structure and projected density of states (PDOS) of the One-UC slab exhibit a clear metallic character, as shown in Figure 2(a). The electronic states near the Fermi level (E_F) are primarily composed of Ni$-d_{x^2-y^2}$ and Ni$-d_{z^2}$ orbitals, which are well separated from the lower-energy Ni-t_{2g} orbitals. Moreover, these Ni$-d$ orbitals exhibit hybridization with O$-p$ orbitals within the energy range of -2 eV to 2 eV. Due to interlayer hybridization, the Ni$-d_{z^2}$ electronic states form bonding and antibonding bands, located below and above E_F, respectively. Additionally, the La-derived states make minimal contributions to the electronic states at E_F. The electronic structures of the Three-UC slab exhibit a similar behavior to that of the One-UC slab, as shown in Supplementary Figure 1(a). Notably, the reduced structural symmetry in thin films induces a splitting of Ni-d_{z^2} bonding bands along the $M-\Gamma$ direction, leading to the formation of distinct electronic pockets near the near the M point [See Figure 3(a)]. In contrast, the Half-UC slab, which retains higher structural symmetry, does not exhibit such splitting in the Ni-d_{z^2} bonding bands [see Figure 2(b)].

For U_{eff} = 2 eV, the Ni$-d_{z^2}$ bonding bands shift downward and approach E_F. Consequently, the density of states of Ni$-d_{z^2}$ attains a maximum at E_F in the One-UC slab, as shown in Figure 2(c). A similar downward shift is observed in the electronic structure of the Three-UC slab, where the Ni$-d_{z^2}$ bonding bands move closer to E_F, as demonstrated in Supplementary Figure 1 (b). This behavior corresponds to the metallization of the lower σ bonds in the high-presure phase of bulk $La_3Ni_2O_7$. These results indicate that the electronic structure of $La_3Ni_2O_7$ thin films closely resembles that of the high-pressure phase of the bulk material, which may provide insight into the emergence of high-temperature superconductivity in thin films. In contrast, the E_F in the Half-UC slab exhibits only a slight downward shift, as illustrated in Figure 2(d). Previous studies on bulk $La_3Ni_2O_7$ have reported that DFT calculations with U_{eff} =

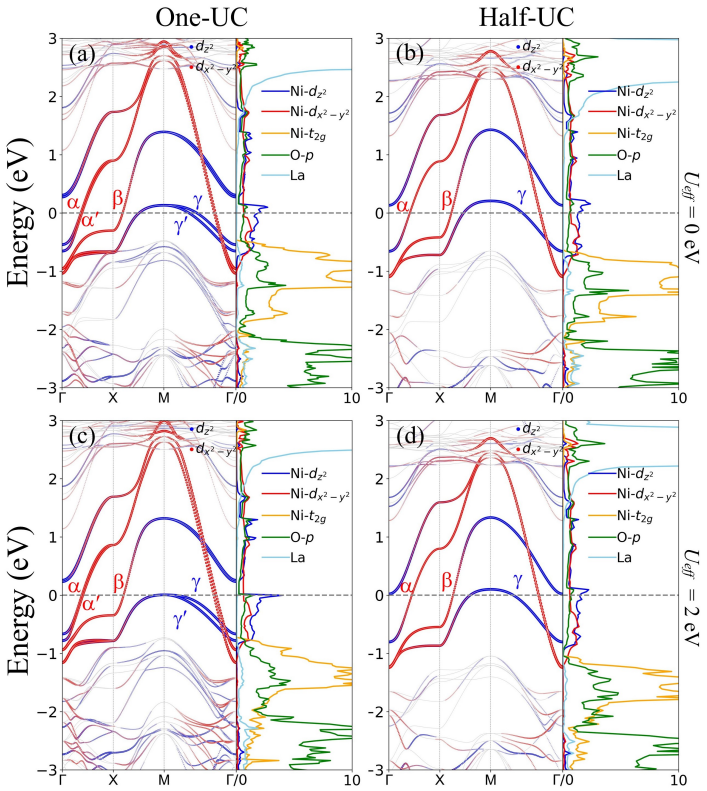

Figure 2 DFT-calculated band structures and partial density of states (PDOS) of $La_3Ni_2O_7$ thin films. Panels (a) and (b) correspond to calculations with $U_{eff} = 0$ eV, and panels (c) and (d) correspond to $U_{eff} = 2$ eV. The contributions from the Ni$-d_{x^2-y^2}$ and d_{z^2} orbitals are highlighted in blue and red, respectively, while Ni$-t_{2g}$, O-p, and La states are represented in orange, green, and cyan, respectively. The Fermi level (E_F) is set to 0 eV. Here, U_{eff} denotes the effective hubbard parameter, and UC represents unit cell.

3.5 eV yield results that are in good agreement with experimental observations [39]. To further explore this, we also consider the case of $U_{eff} = 3.5$ eV. Under this condition, the Ni$-d_{z^2}$ bonding bands in the Three-UC and One-UC slabs shift further downward, moving below E_F, as shown in Supplementary Figures. 1(c) and 2(a). However, in the Half-UC slab, E_F still crosses the Ni$-d_{z^2}$ bonding bands, as shown in Supplementary Figure 2(b).

Figure 3 presents the evolution of the Fermi surface in $La_3Ni_2O_7$ thin films under different slab configurations and Hubbard U_{eff}. Panels (a) and (c) correspond to $U_{eff} = 0$ eV, while panels (b) and (d) correspond to $U_{eff} = 2$ eV. For $U_{eff} = 0$ eV, the Fermi surface of the One-UC slab consists of three electron pockets (α, α', β) and two hole pockets (γ, γ'), as shown in Figure 3(a). Notably, the γ and γ' pockets are primarily derived from the Ni$-d_{z^2}$ orbital. The splitting of the Ni-d_{z^2} and Ni$-d_{x^2-y^2}$ states along the $M - \Gamma$ and $X - \Gamma$ directions gives rise to the additional α' and γ' pockets. This splitting originates from inter-stack interactions induced by the reduced

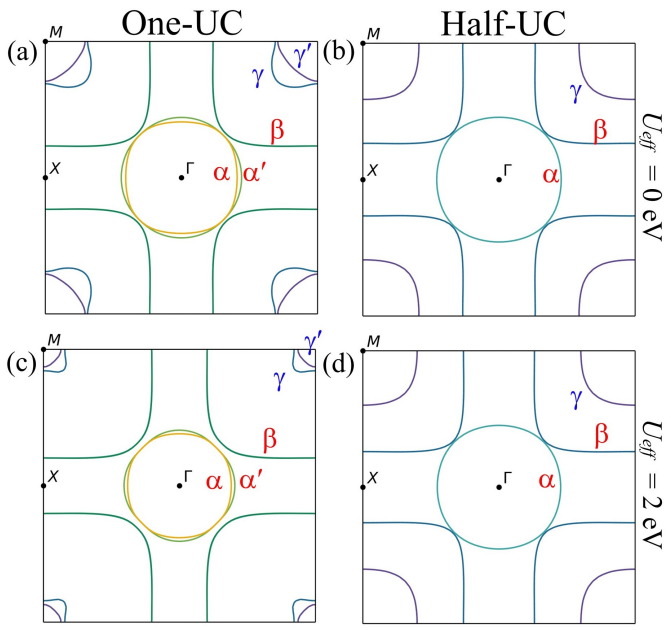

Figure 3 DFT-calculated two-dimensional Fermi surfaces of $La_3Ni_2O_7$ thin films for different slab models. Panels (a) and (c) correspond to the One-UC structure, while panels (b) and (d) corresponds to the Half-UC structure. The upper panels show results obtained with $U_{eff} = 0$ eV, and the lower panels correspond to $U_{eff} = 2$ eV. Here, U_{eff} denotes the effective hubbard parameter, and UC represents unit cell.

structural symmetry in thin films. In contrast, there are two electron pockets (α, β) and one hole pocket (γ) on the Fermi surface in the Half-UC slab, as shown in Figure 3(b).

For $U_{eff} = 2$ eV, as the Ni$-d_{z^2}$ bonding bands in the One-UC slab shift downward and approach E_F, there is a significant reduction in the spatial extent of the hole pokets γ and γ' around the M point in the Brillouin zone, as shown in Figure 3(c). In contrast, the Fermi surface geometry in the Half-UC slab exhibits minimal changes, as depicted in Figure 3(d).

2.3 Two-orbital models

Based on the previous subsections, the thickness of the slab model significantly influences the Ni-O bond lengths, which in turn affect the electronic structure. Experimental samples typically have a thickness of One-UC–Three-UC, and calculations for the Three-UC slab are expected to more closely reflect the experimental conditions. However, due to the complexity of the Three-UC slab model, we have chosen to construct the tight-binding (TB) model using the One-UC slab, which captures the main features of the electronic band structure observed in the Three-UC slab. The Half-UC slab is also considered for comparison.

Building on the electronic structures obtained from our DFT calculations, we first focus on the double-stacked two-orbital model for the One-UC slab. This model incorporates the Ni$-d_{x^2-y^2}$ and Ni$-d_{z^2}$ orbitals within the framework of the maximally

Table 2 Hopping parameters for the One-UC slab model of $La_3Ni_2O_7$ thin films. $t^x_{A/B,[00]}$ and $t^z_{A/B,[00]}$ represent the site energies for the $d_{x^2-y^2}$ and d_{z^2} orbitals in layer A and B, repectively. The numbers in the brackets correspond to parameters of the high-pressure phase of bulk $La_3Ni_2O_7$ [3]. The units are eV.

Index	Layer	i	j	$t^x_{[ij]}$	$t^z_{[ij]}$	$t^{xz}_{[ij]}$
Stack 1	A	0	0	0.844(0.776)	0.519(0.409)	0.000
		1	0	-0.462(-0.483)	-0.134(-0.110)	0.228(0.239)
		1	1	0.075(0.069)	-0.021(-0.017)	0.000
		2	0	-0.053	-0.008	0.017
		3	0	-0.013	-0.003	0.000
	B	0	0	0.918	0.344	0.000
		1	0	-0.460	-0.083	0.201
		1	1	0.075	-0.015	0.000
		2	0	-0.055	-0.013	0.023
		3	0	-0.012	-0.002	0.000
	AB	0	0	0.005(0.005)	-0.550(-0.635)	0.000
		1	0	-0.000	0.020	-0.031(-0.034)
Stack 2	A	0	0	0.918	0.344	0.000
		1	0	-0.460	-0.083	0.201
		1	1	0.075	-0.015	0.000
		2	0	-0.055	-0.013	0.023
		3	0	-0.012	-0.002	0.000
	B	0	0	0.844	0.519	0.000
		1	0	-0.462	-0.134	0.228
		1	1	0.075	-0.021	0.000
		2	0	-0.053	-0.008	0.017
		3	0	-0.013	-0.003	0.000
	AB	0	0	0.005	-0.550	0.000
		1	0	0.000	0.020	-0.029

localized Wannier functions Hamiltonian. The total Hamiltonian is given by

$$\begin{aligned} \mathcal{H} &= \mathcal{H}_0 + \mathcal{H}_U, \\ \mathcal{H}_0 &= \sum_{\mathrm{k}\sigma} \Psi^\dagger_{\mathrm{k}\sigma} H(\mathrm{k}) \Psi_{\mathrm{k}\sigma}. \end{aligned} \tag{1}$$

Here $\mathcal{H}_0$ denotes the TB Hamiltonian derived from the Wannier downfolding procedure, while $\mathcal{H}_U$ represents the Coulomb interaction term [56].

The basis of the model is defined as $\Psi_\sigma = (d_{1Ax\sigma}, d_{1Az\sigma}, d_{1Bx\sigma}, d_{1Bz\sigma}, d_{2Ax\sigma}, d_{2Az\sigma}, d_{2Bx\sigma}, d_{2Bz\sigma})^T$, where the field operator $d_{s\sigma}$ annihilates an electron in the state s with spin σ. The indices are assigned as follows: 1/2 label the stacked layers, A/B correspond to the bilayer sublattices, and x/z denote the $d_{x^2-y^2}$ and d_{z^2} orbitals, respectively. The labeling convention is illustrated in Figure 1(b).

Table 3 Hopping parameters for Half-UC slab model of $La_3Ni_2O_7$ thin films. $t^x_{A,[00]}$, $t^z_{A,[00]}$ are the site energies for $d_{x^2-y^2}$ and d_{z^2} orbitals in layer A. The units are eV.

Index	Layer	i	j	$t^x_{[ij]}$	$t^z_{[ij]}$	$t^{xz}_{[ij]}$
Stack 1	A	0	0	0.756	0.389	0.000
		1	0	-0.445	-0.131	0.221
		1	1	0.060	-0.015	0.000
		2	0	-0.057	-0.011	0.019
		3	0	-0.009	-0.004	0.000
	AB	0	0	0.000	-0.503	0.000
		1	0	0.000	0.026	-0.031

The TB Hamiltonian $H(\mathrm{k})$ takes the form

$$
\begin{aligned}
H(\mathrm{k}) &= \begin{pmatrix} H^1(\mathrm{k}) & H^{12}(\mathrm{k}) \\ H^{12}(\mathrm{k}) & H^2(\mathrm{k}) \end{pmatrix}, \\
H^{1/2}(\mathrm{k}) &= \begin{pmatrix} H^{1/2}_A(\mathrm{k}) & H^{1/2}_{AB}(\mathrm{k}) \\ H^{1/2}_{AB}(\mathrm{k}) & H^{1/2}_B(\mathrm{k}) \end{pmatrix}, \\
H^{1/2}_{A/B}(\mathrm{k}) &= \begin{pmatrix} H^{1/2,x}_{A/B}(\mathrm{k}) & H^{1/2,xz}_{A/B}(\mathrm{k}) \\ H^{1/2,xz}_{A/B}(\mathrm{k}) & H^{1/2,z}_{A/B}(\mathrm{k}) \end{pmatrix}, \\
H^{1/2}_{AB}(\mathrm{k}) &= \begin{pmatrix} H^{1/2,x}_{AB}(\mathrm{k}) & H^{1/2,xz}_{AB}(\mathrm{k}) \\ H^{1/2,xz}_{AB}(\mathrm{k}) & H^{1/2,z}_{AB}(\mathrm{k}) \end{pmatrix}.
\end{aligned} \tag{2}
$$

The matrix elements are defined as follows:

$$
\begin{aligned}
H^{1/2,x/z}_{A/B}(\mathrm{k}) =& 2t^{1/2,x/z}_{A/B,[1,0]} \left(\cos k_x + \cos k_y\right) \\
&+2t^{1/2,x/z}_{A/B,[2,0]} \left(\cos 2k_x + \cos 2k_y\right) \\
&+2t^{1/2,x/z}_{A/B,[3,0]} \left(\cos 3k_x + \cos 3k_y\right) \\
&+4t^{1/2,x/z}_{A/B,[1,1]} \cos k_x \cos k_y + \epsilon^{1/2,x/z}_{A/B}, \\
H^{1/2,xz}_{A/B}(\mathrm{k}) =& 2t^{1/2,xz}_{A/B,[1,0]} \left(\cos k_x - \cos k_y\right) \\
&+2t^{1/2,xz}_{A/B,[2,0]} \left(\cos 2k_x - \cos 2k_y\right), \\
H^{1/2,x/z}_{AB}(\mathrm{k}) =& t^{1/2,x/z}_{AB,[0,0]} + 2t^{1/2,x/z}_{AB,[1,0]} \left(\cos k_x + \cos k_y\right), \\
H^{1/2,xz}_{AB}(\mathrm{k}) =& 2t^{1/2,xz}_{AB,[1,0]} \left(\cos k_x - \cos k_y\right), \\
H^{12,z}_{AB}(\mathrm{k}) =& 4t^{12,z}_{AB}[\cos(k_x/2)\cos(k_y/2)].
\end{aligned}
$$

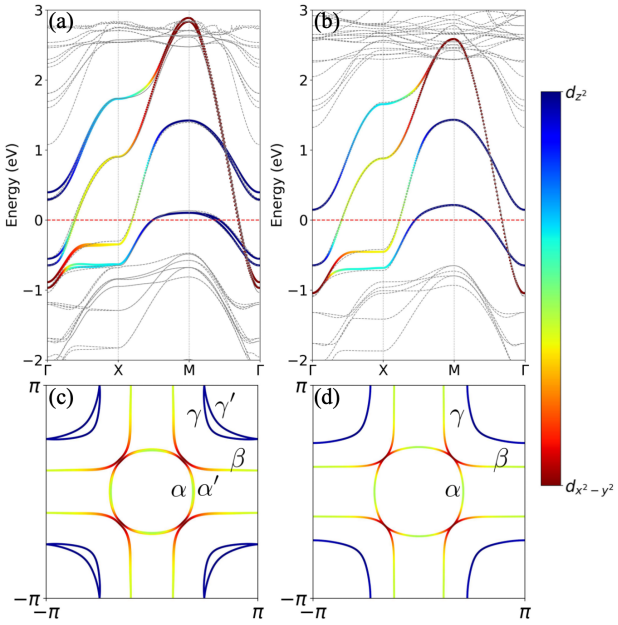

Figure 4 Band structures and Fermi surfaces of the two-obital models for $La_3Ni_2O_7$ thin films. Panels (a) and (c) correspond to the double-stacked two-orbital model for the One-UC slab, while panels (b) and (d) correspond to the single-stacked two-orbital model for the Half-UC slab. The color bar indicates the orbital weights, with red and blue represent $d_{x^2-y^2}$ and d_{z^2}, respectively. In panels (a) and (b), the gray lines represent the DFT-calculated band structures with $U_{eff} = 0$ eV. The E_F is set to 0 eV. Here, U_{eff} denotes the effective hubbard parameter, and UC represents unit cell.

Here $H_{A/B}^{1/2,x/z}(\mathrm{k})$ and $H_{AB}^{1/2,x/z}(\mathrm{k})$ describe intralayer and interlayer hopping within the same orbitals ($d_{x^2-y^2}$ or d_{z^2}), respectively, while $H_{A/B}^{1/2,xz}(\mathrm{k})$ and $H_{AB}^{1/2,xz}(\mathrm{k})$ represent intralayer and interlayer hybridization between $d_{x^2-y^2}$ and d_{z^2} orbitals. Additionally, $H_{AB}^{12,z}(\mathrm{k}) = 4t_{AB}^{12,z}\cos(k_x/2)\cos(k_y/2)$ describes inter-stack hopping within the d_{z^2} orbital, with a corresponding hopping parameter $t_{AB}^{12,z} = -0.025$. Hopping parameters for the One-UC slab model of $La_3Ni_2O_7$ thin film are summarized in Table 2.

For the single-stacked two-orbital model of the Half-UC slab, the system exhibits layer symmetry and the absence of inter-stack coupling, as characterized by the conditions $H^1(\mathrm{k}) = H^2(\mathrm{k})$, $H^{12}(\mathrm{k}) = 0$, and $H_A^1(\mathrm{k}) = H_B^1(\mathrm{k})$. These conditions indicate that the Hamiltonians of the individual layers are identical, there is no direct coupling between the stacks, and the interfacial hopping parameters are equivalent for both sublattices. The corresponding hopping parameters for the Half-UC slab model of $La_3Ni_2O_7$ thin film are provided in Table 3.

Using the TB parameters listed in Tables 2 and 3, we present the resulting band structure and Fermi surface for both One-UC and Half-UC slabs. As shown in Figure 4(a), the model for the One-UC slab accurately reproduces the DFT band structure near the E_F. Notably, we observe a splitting of the Ni-d_{z^2} bonding bands along the $M - \Gamma$ direction, which originates from inter-stack interaction, specifically $t_{AB}^{12,z}$. Regarding the Fermi surface, we identify three electron pockets α, α', β and two hole

pockets γ, γ', as illustrated in Figure 4(c). The $\alpha, \alpha', \beta-$pocket exhibit mixed orbital character, while the $\gamma, \gamma'-$pockets are primarily dominated by the d_{z^2} orbital state. Our results indicate that the electronic structure of $La_3Ni_2O_7$ thin film at ambient pressure closely resembles that of the high-pressure bulk phase. A key structural aspect is the in-plane lattice constant of the thin film, which is $3.77\mathring{A}$–large than the pseudo-tetragonal bulk value of $3.715\mathring{A}$. This lattice expansion may account for the lower T_c of the thin film compared to the bulk, suggesting that strain engineering could be a viable approach to enhancing T_c by further compressing the in-plane lattice constant. Furthermore, we note that the interlayer hopping amplitude $t^z_{AB,[00]} = -0.550$ is 1.19 times larger than the intralayer nearest-neighbor hopping $t^x_1 = -0.462$. However, it remains 13.4% smaller than its bulk counterpart ($t^z_{AB,[00]} = -0.635$). This reduction in interlayer coupling suggests a possible weakening of unconventional pairing in the thin film compared to the bulk.

For the Half-UC slab model, no splitting in the Ni-d_{z^2} bonding bands (See Figure 4(b)). Consequently, the Fermi surface consists of two electron pockets α, β and one hole pocket γ, as illustrated in Figure 4(d). Additionally, the interlayer hopping amplitude $t^z_{AB,[00]} = -0.503$ is 1.13 times larger than the intralayer nearest-neighbor hopping $t^x_1 = -0.445$, yet it remains 21% smaller than its bulk counterpart. Notably, when we set $t^{12,z}_{AB} = 0$, no splitting is observed in the band structure or the Fermi surface of the One-UC slab, as shown in Supplementary Figure 3.

2.4 High-energy *dp* models

To incorporate the effects of $O-p$ orbitals, we introduce high-energy dp models: a double-stacked eleven-orbital model for the One-UC slab (referred to as twenty-two-orbital model) and a single-stacked eleven-orbital model for the Half-UC slab (referred to as the eleven-orbital model). In both models, the basis for Stack 1 is given by $\Psi = (d_{Az}, d_{Bz}, d_{Ax}, d_{Bx}, d_{Ap_x}, d_{Bp_x}, d_{Ap_y}, d_{Bp_y}, d_{p_z}, d_{p_{z'}}, d_{p_{z''}})^T$, which includes four in-plane orbitals $(p_{Ax}, p_{Ay}, p_{Bx}, p_{By})$ and three apical orbitals $(p_z, p_{z'}, p_{z''})$, as illustrated in Supplementary Figure 4. Here, A and B denote the bilayer sublattices.

The TB parameters of the twenty-two-orbital model are listed in Table 4, while those of the eleven-orbital model are provided in Table 5. Due to the symmetry between Stack 1 and Stack 2, only the parameters for Stack 1 are presented, and inter-stack hopping terms are not considered. Both models incorporate hopping interactions arising from pd, pp orbital overlaps. Based on the TB parameters, we present the resulting band structure and Fermi surface for both the One-UC and Half-UC slabs, as shown in Figure 5. The resulting band structure in Figure 5 covers an energy range akin to that of Figure 4 and can also reproduce the main features at E_F. Furthermore, we find a hopping of 1.296 for eleven-orbital model and of 1.304/1.105 for twenty-two-orbital model between d_{z^2} orbital and two apical $p_{z'}, p_{z''}$ orbitals, which are crucial in estimating effective interlayer d_{z^2} spin exchange coupling. The high-energy models would provide a foundation for further investigations of magnetic exchange coupling and electronic correlations.

Table 4 TB parameters for Wannier downfolding of the twenty-two-orbital model. Only the parameters of Stack 1 are presented, due to the symmetry between Stack 1 and Stack 2. See the schematic in Supplementary Figure 4 for further details.

Stack 1			
Hopping	$Ad_{z^2} - p_{z'}$	$Ad_{z^2} - p_z$	$Ad_{z^2} - Ap_{x/y}$
	1.304	-1.478	0.692
Hopping	$Bd_{z^2} - p_{z''}$	$Bd_{z^2} - p_z$	$Bd_{z^2} - Bp_{x/y}$
	-1.105	1.435	0.629
Hopping	$Ap_x - Ap_y$	$Ap_{x/y} - p_z$	$Ap_{x/y} - p_{z'}$
	-0.560	-0.435	0.443
Hopping	$Bp_x - Bp_y$	$Bp_{x/y} - p_z$	$Bp_{x/y} - p_{z''}$
	-0.575	0.428	-0.380
Hopping	$Ad_{x^2-y^2} - Ap_{x/y}$	$Bd_{x^2-y^2} - Bp_{x/y}$	
	$\pm$1.480	$\pm$1.479	
Site	Ad_{z^2}/Bd_{z^2}	$Ad_{x^2-y^2}/Bd_{x^2-y^2}$	p_z
Energy	-1.104/-1.036	-1.001/-0.9223	-4.078
Site	$Ap_{x/y}/Bp_{x/y}$	$Ap_{z'}/Bp_{z''}$	
Energy	-4.669/-4.630	-2.730/-3.224	

2.5 Spin susceptibility for two-orbital models

With the multi-orbital Hubbard model defined above, we investigate the magnetic response and Fermi surface nesting by calculating the spin susceptibility at the RPA level. Given that inter-stack hoppings are weak, we neglect them in our analysis. The resulting Fermi surface and energy bands in the absence of inter-stack hopping are provided in the Supplementary Figure 3.

To better demonstrate the Fermi surface nesting relations associated with the bilayer structure, we define the even and odd magnetic susceptibilities as: $\chi^{e/o} = \chi_{||} \pm \chi_{\perp}$, with $\chi_{||}$ and $\chi_{\perp}$ representing intralayer and interlayer contributions, respectively. The definitions and computational details are available in the Methods section. Physically, it is easily proved that the χ^e originates from nestings within the bonding (α, γ) and within the antibonding (β) bands, while χ^o originates solely from nestings between the bonding and antibonding bands [57].

Figure 6 presents the static RPA spin susceptibility $\chi^{e/o}(\mathbf{q}, \omega = 0)$ for the double-stacked two-orbital model, computed with $U = 0.7$ eV, $J_H = 0.2$ eV, and temperature $T = 0.1$ K. In the even channel, we observe a strong response near the X point,

Table 5 TB parameters for the Wannier downfolding of the eleven-orbital model. Only the parameters of Layer A are presented, due to the symmetry between Layers A and B. See the schematic in Supplementary Figure 4 for further details.

Stack 1				
Hopping	$Ad_{z^2} - p_z$	$Ad_{z^2} - p_{z'}$	$Ad_{z^2} - Ap_{x/y}$	$Ad_{x^2-y^2} - Ap_{x/y}$
	-1.423	1.296	0.697	$\pm$1.482
Hopping	$Ap_x - Ap_y$	$Ap_{x/y} - p_z$	$Ap_{x/y} - p_{z'}$	
	-0.589	0.483	-0.440	
Site	Ad_{z^2}	$Ad_{x^2-y^2}$	$Ap_{x/y}$	p_z
energy	-1.198	-1.127	-4.790	-4.150
Site	$Ap_{z'/z''}$			
energy	-2.927			

indicating nesting within the γ pocket, along with additional nesting within the β pocket. In the odd channel, nesting is evident between the β and γ pockets, as well as between the α and β pockets.

Figure 7 presents the spin susceptibility for the single-stacked two-orbital model, calculated using $U = 0.8$ eV, $J_H = 0.2$ eV and $T = 0.1$ K . The Fermi surface nesting patterns in the odd channel closely resemble those of the double-stacked model. In the even channel, nesting primarily occurs within the γ and β pockets, whereas in the odd channel, significant nesting is observed between the γ and β pockets, as well as between the α and β pockets. The observed differences in $\chi^{e/o}$ between the double-stacked and single-stacked models can be attributed to their distinct Fermi surface geometries.

3 Methods

3.1 First-principles calculations

Our first-principles calculations are performed using the DFT as implemented in the Vienna *ab initio* simulation package (VASP) [58, 59]. The exchange-correlation interactions are treated within the generalized gradient approximation (GGA) using the Perdew-Burke-Ernzerhof (PBE) functional [60]. The projector augmented-wave (PAW) method [61] is employed with a plane-wave cutoff energy of 600 eV. Structural relaxation and electronic self-consistent calculations are conducted on a Γ-centered $12 \times 12 \times 1$ $k-$points mesh using the Monkhorst-Pack scheme, while a denser $k-$points grid of $27 \times 27 \times 1$ is used for Fermi surface calculations. The atomic positions are fully relaxed until the residual forces on each atom are less than 0.005 eV/$\mathring{A}$, and the electronic self-consistency convergence criterion is set to 10^{-6} eV. The optimized atomic

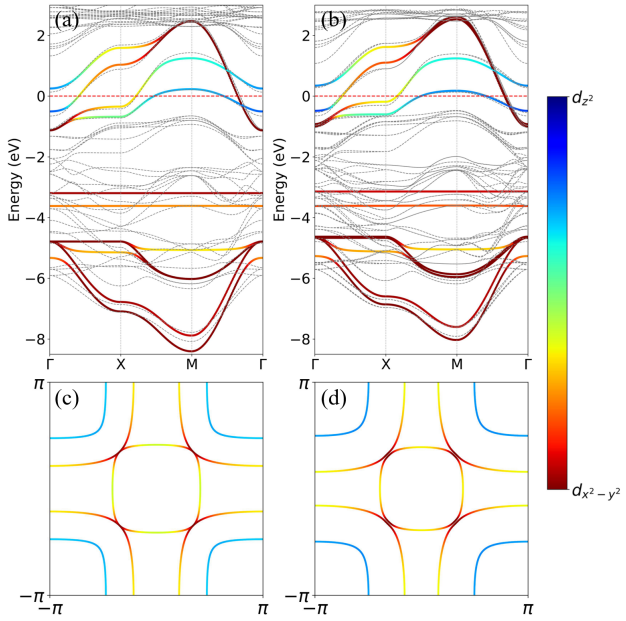

Figure 5 Band structures and Fermi surfaces of High-energy *dp* models including oxeygen orbitals for $La_3Ni_2O_7$ thin films. Panels (a) and (c) correspond to the eleven-orbital model for the Half-UC slab, while panels (b) and (d) correspond to the twenty-two-orbital model for the One-UC slab. The color bar indicates the orbital weights, with red and blue represent $d_{x^2-y^2}$ and d_{z^2}, respectively. In panels (a) and (b), the gray lines represent the DFT-calculated band structures with $U_{eff} = 0$ eV. The E_F is set to 0 eV. Here, U_{eff} denotes the effective hubbard parameter, and UC represents unit cell.

coordinates are provided in Supplementary Data 1 and 2 for the Half-UC structure with $U_{eff} = 0$ and 2 eV, respectively, and in Supplementary Data 3 and 4 for One-UC structure with $U_{eff} = 0$ and 2 eV, respectively.

To construct effective models, maximally localized Wannier functions are obtained using the Wannier90 code [62–64]. For DFT + U calculations [65], an effective Hubbard U_{eff} is applied to the Ni $3d$ orbitals.

3.2 Hamiltonian of high-energy *dp* models

For the twenty-two-orbital model, we do not consider the hoppings between orbitals in different stacks. So the hamiltonian of twenty-two-orbital model take the same form as the one for the eleven-orbital model. Here we show the TB hamiltonian for high-energy *dp* models [3]. The basis here is $(Ad_z, Bd_z, Ad_x, Bd_x, Ap_x, Bp_x, Ap_y, Bp_y, p_z, p_{z'}, p_{z''})$. The position of these orbitals can be seen in Supplementary Figure 4. Here we show the elements of Hamiltonian $H(\alpha, \beta)$

$$
\begin{aligned}
H(1,9) = t^{Ad_z,p_z}, H(2,9) = t^{Bd_z,p_z}, H(1,10) = t^{Ad_z,p_{z'}}, H(2,11) = t^{Bd_z,p_{z''}}, \qquad (3)\\
H(3,5) = -2\mathrm{i}t^{Ad_x,Ap_x}\sin(0.5k_x), \quad H(3,7) = -2\mathrm{i}t^{Ad_x-Ap_y}\sin(0.5k_y),\\
H(4,6) = -2\mathrm{i}t^{Bd_x,Bp_x}\sin(0.5k_x), \quad H(4,8) = -2\mathrm{i}t^{Bd_x-Bp_y}\sin(0.5k_y),
\end{aligned}
$$

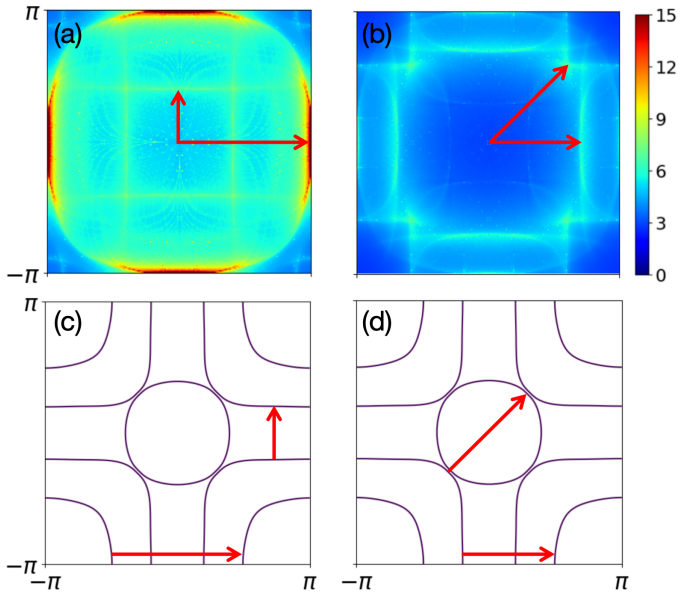

Figure 6 RPA spin susceptibilities of even and odd channel, and illustration of Fermi surfaces nesting in the double-stacked two-orbital model. Panels (a) and (b) show the even channel (χ^e) and odd channel (χ^o) susceptibilities for the double-stacked two-orbital model, respectively, calculated with intraorbital Coulomb interaction $U = 0.7$ eV and Hund's coupling $J_H = 0.2$ eV at a temperature $T = 0.1$ K. Panels (c) and (d) depict the Fermi surfaces, where red arrows indicating the nesting vectors.

$$
\begin{aligned}
H(1,5) &= -2\mathrm{i}t^{Ad_z,Ap_x}\sin(0.5k_x), \quad H(1,7) = -2\mathrm{i}t^{Ad_z-Ap_y}\sin(0.5k_y),\\
H(2,6) &= -2\mathrm{i}t^{Bd_z,Bp_x}\sin(0.5k_x), \quad H(2,8) = -2\mathrm{i}t^{Bd_z-Bp_y}\sin(0.5k_y),\\
H(5,7) &= 4t^{Ap_x-Ap_y}\sin(0.5k_x)\sin(0.5k_y),\\
H(6,8) &= 4t^{Bp_x-Bp_y}\sin(0.5k_x)\sin(0.5k_y),\\
H(5,9) &= -2\mathrm{i}t^{Ap_x,p_z}\sin(0.5k_x), \quad H(7,9) = -2\mathrm{i}t^{Ap_y,p_z}\sin(0.5k_y),\\
H(6,9) &= -2\mathrm{i}t^{Bp_x,p_z}\sin(0.5k_x), \quad H(8,9) = -2\mathrm{i}t^{Bp_y,p_z}\sin(0.5k_y),\\
H(5,10) &= -2\mathrm{i}t^{Ap_x,p_{z'}}\sin(0.5k_x), \quad H(7,10) = -2\mathrm{i}t^{Ap_y,p_{z'}}\sin(0.5k_y),\\
H(6,11) &= -2\mathrm{i}t^{Bp_x,p_{z''}}\sin(0.5k_x), \quad H(8,11) = -2\mathrm{i}t^{Bp_y,p_{z''}}\sin(0.5k_y).
\end{aligned}
$$

The elements $H(\beta,\alpha)$ can be obtained by $H(\beta,\alpha) = H(\alpha,\beta)^*$. The diagnal elements are site energies which can be found in Table 4 and Table 5.

3.3 Calculation of spin susceptibility

Upon determining the hopping parameters of the TB models and incorporating electron interactions, we construct a multi-orbital Hubbard model as Equation 1 without

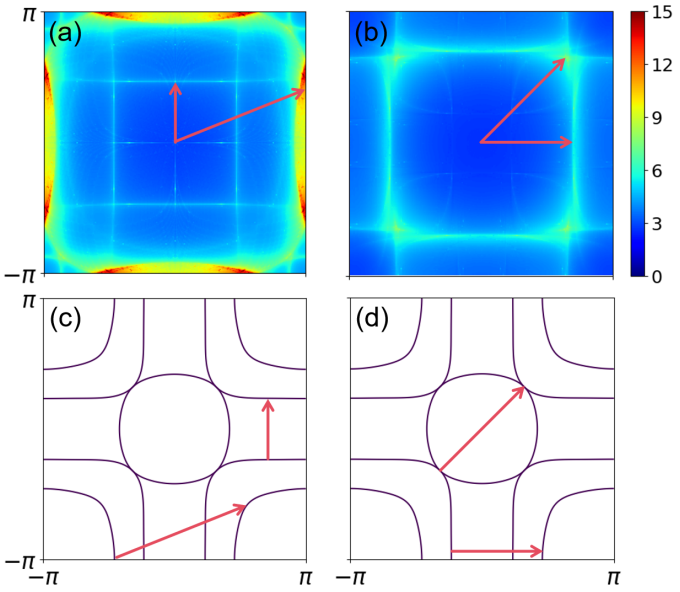

Figure 7 RPA spin susceptibility of even and odd channel, and illustration of Fermi surfaces nesting in the single-stacked two-orbital model. Panels (a) and (b) show the even channel (χ^e) and odd channel (χ^o) susceptibilities for the single-stacked two-orbital model, respectively, calculated with intraorbital Coulomb interaction $U = 0.8$ eV and Hund's coupling $J_H = 0.2$ eV at a temperature $T = 0.1$ K. Panesls (c) and (d) present the Fermi surfaces, where red arrows indicating the nesting vectors.

considering hoppings between two stacks.

$$\begin{aligned}\mathcal{H}_U =& U\sum_{is} n_{is\uparrow}n_{is\downarrow} \\ &+(U'-J_H\delta_{\sigma\sigma'})\sum_{i\sigma\sigma'}(n_{iAx\sigma}n_{iAz\sigma'}+n_{iBx\sigma}n_{iBz\sigma'}) \\ &+J_H\sum_{i\sigma}\sum_{\mu}^{A,B}(d^\dagger_{i\mu x\sigma}d^\dagger_{i\mu z\bar{\sigma}}d_{i\mu x\bar{\sigma}}d_{i\mu z\sigma} \\ &+d^\dagger_{i\mu x\sigma}d^\dagger_{i\mu x\bar{\sigma}}d_{i\mu z\bar{\sigma}}d_{i\mu z\sigma}+h.c.).\end{aligned} \tag{4}$$

The TB Hamiltonian $\mathcal{H}_0$ is expressed with the basis $\Psi_\sigma = (d_{Ax\sigma}, d_{Az\sigma}, d_{Bx\sigma}, d_{Bz\sigma})$, where $d_{s\sigma}$ is the annihilation operator for an electron in the state $s = (Ax, Az, Bx, Bz)$ with spin σ. The interaction parameters include U (intraorbital Coulomb interaction), U' (interorbital Coulomb interaction) and J_H (Hund's coupling). Kanamori relation is applied here, given by $U' = U - 2J_H$ [66].

In general, the bare (non-interaction) susceptibility is defined as

$$\chi^0_{\alpha\beta\gamma\delta}(\mathrm{q},\omega) = -\frac{1}{N_\mathrm{k}}\sum_{\mathrm{k},mn}\frac{f_F(\varepsilon^m_\mathrm{k})-f_F(\varepsilon^n_{\mathrm{k+q}})}{\mathrm{i}\omega+\varepsilon^m_\mathrm{k}-\varepsilon^n_{\mathrm{k+q}}}$$

$$U_{\delta m}(\mathrm{k})U^*_{\alpha m}(\mathrm{k})U_{\beta n}(\mathrm{k}+\mathrm{q})U^*_{\gamma n}(\mathrm{k}+\mathrm{q}). \tag{5}$$

with the band indices m, n and the Fermi-Dirac distribution function $f_F(\varepsilon_{\mathbf{k}}) = 1/(\mathrm{e}^{\varepsilon_{\mathbf{k}}/T}+1)$. The matrix element $U_{\delta m}(\mathrm{k})$ represents the eigenvector connecting orbital δ and band m at wave vector k. At the RPA level, the spin channel interaction vertex is defined as

$$\Gamma^m_{\alpha\beta\gamma\delta} = \begin{cases} U & \alpha=\beta=\gamma=\delta, \\ U' & \alpha=\delta\neq\beta=\gamma, \\ J_H & \alpha=\beta\neq\gamma=\delta, \\ J' & \alpha=\gamma\neq\beta=\delta. \end{cases} \tag{6}$$

Here pair hopping J' satisfies $J' = J_H$. The RPA spin susceptibility is then computed in a matrix-product form as

$$\chi^S_{(\alpha\beta,\delta\gamma)} = \left[I - \chi^0\Gamma^m_{(\alpha\beta,\delta\gamma)}\right]^{-1}\chi^0_{(\alpha\beta,\delta\gamma)}. \tag{7}$$

Considering the bilayer structure of $La_3Ni_2O_7$, the interlayer hopping terms in the Hamiltonian acquire a phase factor of $\mathrm{e}^{\mathrm{i}k_z}$ due to the k_z-dependence. Here, k_z can take values of either 0 or π. When contracting the orbital indices to compute the spin susceptibility, we define the in-plane and interlayer susceptibilities as $\chi_{||} = \sum_{\alpha\beta}(\chi_{A\alpha A\beta} + \chi_{B\alpha B\beta})$ and $\chi_\perp = \sum_{\alpha\beta}(\chi_{A\alpha B\beta} + \chi_{B\alpha A\beta})$, where $\chi_{\alpha\beta} = \chi_{\alpha\alpha\beta\beta}$ with orbital indices contracted. For $k_z = 0$, the phase factor $\mathrm{e}^{\mathrm{i}0} = 1$, and the spin susceptibility is given by $\chi^e = \chi_{||} + \chi_\perp$. Conversely, for $k_z = \pi$, the phase factor $\mathrm{e}^{\mathrm{i}\pi} = -1$, leading to a spin susceptibility of $\chi^o = \chi_{||} - \chi_\perp$. In the even channel χ^e, Fermi surface nesting which occurs within the bonding/antibonding bands is evident, including the $\alpha-\alpha$, $\alpha-\gamma$, $\gamma-\gamma$ and $\beta-\beta$ nesting features. In the odd channel χ^o, nesting between bonding and antibonding bands can be observed clearly, such as $\gamma-\beta$, $\alpha-\beta$ [57].

4 Data Availability

The data that support the findings of this study are available from the corresponding author upon reasonable request.

5 Discussion

Our DFT calculations of the thin-film bilayer nickelate superconductors have overall predicted the electronic structure closely resembles the bulk one under pressure, which strongly suggests that they all within the same superconducting mechansim. We note another key aspect to validate this idea, which is the superexchange strength. For the bulk samples, the vertical superexchange between two half-filling d_{z^2} orbitals $J^z_\perp$ is widely believed to be the origin of the superconducting condensation [6, 7]. Here our TB models for the $La_3Ni_2O_7$ thin-film also allow an estimation of the corresponding strengths, which are decreased by ∼24% and ∼36% for single-stacked and double-stacked bilayer nickelates with respect to the pressurized bulk [3], assuming $J^z_\perp \sim (t^z)^2$.

The asymptotic decrease of $J_{\perp}^{z}$ with slab number from our estimation is in line with the notable decrease of T_c from bulk to film as observated in experiments [48, 49], which again reinforce the above general understanding. More profoundly, the consistency indicates an expension of the available experimental techniques for reaching the core of superconducting mechanism in RP nickelates. This is particularly helpful as the exploration on bulk is largely constrained by the exerted pressure. Regrading the role of pressure, on the other hand, the existing evidences on thin-film is also prone to the idea that pressure can help suppressing spin density wave, after which superconducting order is thus to expose. Whereas for the thin-film, due to the higher stability and sniffiness of the $SrLaAlO_4$ substrates, $La_3Ni_2O_7$ lattice is strongly confined to the $I4/mmm$ symmetry without inplane distrostion, which can further prevent the occurance of density waves [48, 49].

On the other hand, it is worth noting that the structural differences between the One-UC and Half-UC slab models–particularly the presence of inter-stack geometry in the One-UC case–lead to more three-dimensional electronic characteristics. In particular, the enhanced interlayer coupling in the One-UC structure gives rise to noticeable out-of-plane (k_z) direction. This suggests that such k_z-dependent features may be experimentally observable in future high-resolution ARPES measurements, providing an additional means to probe the dimensionality and electronic reconstruction in $La_3Ni_2O_7$ thin films.

We note that both experimental and theoretical studies have reported differing results regarding the Fermi surface topology. While Ref.[67] reports a lowering of the Ni-d_{z^2} states under compressive strain, an independent group has observed a d_{z^2}-derived γ-pocket at the Fermi level in $La_2PrNi_2O_7$ thin films, accompanied by a measurable superconducting gap on this pocket [51, 52]. These contrasting observations suggest that the presence or absence of the γ-pocket may be sample-dependent, potentially influenced by factors such as oxygen stoichiometry or subtle strain variations. On the theoretical side, previous studies [68, 69] examined the effect of biaxial strain on bulk nickelates and found that compressive strain tends to increase the apical Ni–O–Ni bond angle toward 180°, consistent with structural features of the high-pressure phase. Other works [70, 71], adopting the lower-pressure Amam phase as a reference and employing DFT + U methods, reported the emergence of d_{z^2}-derived pockets at the Fermi surface under tensile strain. It is well established that the calculated electronic structure of $La_3Ni_2O_7$ is highly sensitive to the choice of the Hubbard U_{eff} parameter (see Supplementary Figure 1). We anticipate that future experimental studies will help resolve these discrepancies and clarify the microscopic origin of the observed differences.

6 Conclusion

In conclusion, we employ slab models for $La_3Ni_2O_7$ thin films that simulate the electronic structure for various thicknesses, including Three-UC, One-UC, and Half-UC. Each slab model incorporates a full unit cell, with the two bilayers referred to as Stack 1 and Stack 2, enabling a detailed examination of the interplay between dimensionality and electronic behaviors. Using density functional theory, we propose a double-stacked

two-orbital effective model of $La_3Ni_2O_7$ thin films, based on the Ni$-e_g$ orbitals. Our analysis reveals the presence of three electron pockets α, α', β and two hole pockets γ, γ' on the Fermi surface, where the additional pockets α' and γ' emerge due to inter-stack interactions. Furthermore, we introduce high-energy models incorporating O$-p$ orbitals to facilitate future studies. Spin susceptibility calculations within the RPA indicate pronounced magnetic correlations primarily driven by nesting effects of the γ pocket, which is predominantly contributed by the Ni$-d_{z^2}$ orbital state. Our results provide theoretical framework for understanding the interplay among dimensionality, magnetism, and superconductivity in $La_3Ni_2O_7$ thin films, offering key insights for future theoretical and experimental research.

References

[1] Sun, H., Huo, M., Hu, X., Li, J., Liu, Z., Han, Y., Tang, L., Mao, Z., Yang, P., Wang, B., *et al.*: Signatures of superconductivity near 80 K in a nickelate under high pressure. Nature **621**(7979), 493–498 (2023) https://doi.org/10.1038/s41586-023-06408-7

[2] Zhu, Y., Peng, D., Zhang, E., Pan, B., Chen, X., Chen, L., Ren, H., Liu, F., Hao, Y., Li, N., Xing, Z., Lan, F., Han, J., Wang, J., Jia, D., Wo, H., Gu, Y., Gu, Y., Ji, L., Wang, W., Gou, H., Shen, Y., Ying, T., Chen, X., Yang, W., Cao, H., Zheng, C., Zeng, Q., Guo, J.-g., Zhao, J.: Superconductivity in pressurized trilayer $La_4Ni_3O_{10-\delta}$ single crystals. Nature **631**(8021), 531–536 (2024) https://doi.org/10.1038/s41586-024-07553-3

[3] Luo, Z., Hu, X., Wang, M., Wú, W., Yao, D.-X.: Bilayer two-orbital model of $La_3Ni_2O_7$ under pressure. Phys. Rev. Lett. **131**(12), 126001 (2023) https://doi.org/10.1103/PhysRevLett.131.126001

[4] Zhang, Y., Lin, L.-F., Moreo, A., Dagotto, E.: Electronic structure, dimer physics, orbital-selective behavior, and magnetic tendencies in the bilayer nickelate superconductor $La_3Ni_2O_7$ under pressure. Phys. Rev. B **108**(18), 180510 (2023) https://doi.org/10.1103/PhysRevB.108.L180510

[5] Lechermann, F., Gondolf, J., Bötzel, S., Eremin, I.M.: Electronic correlations and superconducting instability in $La_3Ni_2O_7$ under high pressure. Phys. Rev. B **108**(20), 201121 (2023) https://doi.org/10.1103/PhysRevB.108.L201121

[6] Luo, Z., Lv, B., Wang, M., Wú, W., Yao, D.-X.: High-T_c superconductivity in $La_3Ni_2O_7$ based on the bilayer two-orbital t-J model. npj Quantum Mater. **9**(1), 1–7 (2024) https://doi.org/10.1038/s41535-024-00668-w

[7] Wú, W., Luo, Z., Yao, D.-X., Wang, M.: Superexchange and charge transfer in the nickelate superconductor $La_3Ni_2O_7$ under pressure. Sci. China Phys. Mech. Astron. **67**(11), 117402 (2024) https://doi.org/10.1007/s11433-023-2300-4

[8] Wang, M., Wen, H.-H., Wu, T., Yao, D.-X., Xiang, T.: Normal and superconducting properties of $La_3Ni_2O_7$. Chin. Phys. Lett. **41**(7) (2024) https://doi.org/10.1088/0256-307X/41/7/077402

[9] Shilenko, D.A., Leonov, I.V.: Correlated electronic structure, orbital-selective behavior, and magnetic correlations in double-layer $La_3Ni_2O_7$ under pressure. Phys. Rev. B **108**(12), 125105 (2023) https://doi.org/10.1103/PhysRevB.108.125105

[10] Yang, Y.-f., Zhang, G.-M., Zhang, F.-C.: Interlayer valence bonds and two-component theory for high-T_c superconductivity of $La_3Ni_2O_7$ under pressure. Phys. Rev. B **108**(20), 201108 (2023) https://doi.org/10.1103/PhysRevB.108.L201108

[11] Huang, J., Wang, Z.D., Zhou, T.: Impurity and vortex states in the bilayer high-temperature superconductor $La_3Ni_2O_7$. Phys. Rev. B **108**(17), 174501 (2023) https://doi.org/10.1103/PhysRevB.108.174501

[12] Christiansson, V., Petocchi, F., Werner, P.: Correlated electronic structure of $La_3Ni_2O_7$ under pressure. Phys. Rev. Lett. **131**(20), 206501 (2023) https://doi.org/10.1103/PhysRevLett.131.206501

[13] Shen, Y., Qin, M., Zhang, G.-M.: Effective bi-layer model hamiltonian and density-matrix renormalization group study for the high-tc superconductivity in $La_3Ni_2O_7$ under high pressure. Chin. Phys. Lett. **40**(12), 127401 (2023) https://doi.org/10.1088/0256-307X/40/12/127401

[14] Oh, H., Zhang, Y.-H.: Type-II $t-J$ model and shared superexchange coupling from hund's rule in superconducting $La_3Ni_2O_7$. Phys. Rev. B **108**(17), 174511 (2023) https://doi.org/10.1103/PhysRevB.108.174511

[15] Liu, Y.-B., Mei, J.-W., Ye, F., Chen, W.-Q., Yang, F.: $s^{\pm}$-wave pairing and the destructive role of apical-oxygen deficiencies in $La_3Ni_2O_7$ under pressure. Phys. Rev. Lett. **131**(23), 236002 (2023) https://doi.org/10.1103/PhysRevLett.131.236002

[16] Liao, Z., Chen, L., Duan, G., Wang, Y., Liu, C., Yu, R., Si, Q.: Electron correlations and superconductivity in $La_3Ni_2O_7$ under pressure tuning. Phys. Rev. B **108**(21), 214522 (2023) https://doi.org/10.1103/PhysRevB.108.214522

[17] Yang, Q.-G., Wang, D., Wang, Q.-H.: Possible $s_{\pm}$-wave superconductivity in $La_3Ni_2O_7$. Phys. Rev. B **108**(14), 140505 (2023) https://doi.org/10.1103/PhysRevB.108.L140505

[18] Chen, C.-Q., Luo, Z., Wang, M., Wú, W., Yao, D.-X.: Trilayer multiorbital models of $La_4Ni_3O_{10}$. Phys. Rev. B **110**, 014503 (2024) https://doi.org/10.1103/PhysRevB.110.014503

[19] Xu, S., Chen, C.-Q., Huo, M., Hu, D., Wang, H., Wu, Q., Li, R., Wu, D., Wang, M., Yao, D.-X., Dong, T., Wang, N.: Origin of the density wave instability in trilayer nickelate $La_4Ni_3O_{10}$ revealed by optical and ultrafast spectroscopy. Phys. Rev. B **111**, 075140 (2025) https://doi.org/10.1103/PhysRevB.111.075140

[20] Yang, J.-J., Yao, D.-X., Wu, H.-Q.: Correlation effects in a simplified bilayer two-orbital hubbard model at half filling. Phys. Rev. B **110**, 235155 (2024) https://doi.org/10.1103/PhysRevB.110.235155

[21] Kaneko, T., Sakakibara, H., Ochi, M., Kuroki, K.: Pair correlations in the two-orbital hubbard ladder: Implications for superconductivity in the bilayer nickelate $La_3Ni_2O_7$. Phys. Rev. B **109**(4), 045154 (2024) https://doi.org/10.1103/PhysRevB.109.045154

[22] Ouyang, Z., Gao, M., Lu, Z.-Y.: Absence of electron-phonon coupling superconductivity in the bilayer phase of $La_3Ni_2O_7$ under pressure. npj Quantum Mater. **9**(1), 1–6 (2024) https://doi.org/10.1038/s41535-024-00689-5

[23] Sakakibara, H., Ochi, M., Nagata, H., Ueki, Y., Sakurai, H., Matsumoto, R., Terashima, K., Hirose, K., Ohta, H., Kato, M., Takano, Y., Kuroki, K.: Theoretical analysis on the possibility of superconductivity in the trilayer ruddlesden-popper nickelate $La_4Ni_3O_{10}$ under pressure and its experimental examination: Comparison with $La_3Ni_2O_7$. Phys. Rev. B **109**, 144511 (2024) https://doi.org/10.1103/PhysRevB.109.144511

[24] Heier, G., Park, K., Savrasov, S.Y.: Competing d_{xy} and $s_{\pm}$ pairing symmetries in superconducting $La_3Ni_2O_7$: LDA + FLEX calculations. Phys. Rev. B **109**(10), 104508 (2024) https://doi.org/10.1103/PhysRevB.109.104508

[25] Zhang, Y., Lin, L.-F., Moreo, A., Maier, T.A., Dagotto, E.: Structural phase transition, s±-wave pairing, and magnetic stripe order in bilayered superconductor $La_3Ni_2O_7$ under pressure. Nat Commun **15**(1), 2470 (2024) https://doi.org/10.1038/s41467-024-46622-z

[26] Zhang, Y., Lin, L.-F., Moreo, A., Maier, T.A., Dagotto, E.: Electronic structure, magnetic correlations, and superconducting pairing in the reduced ruddlesden-popper bilayer $La_3Ni_2O_6$ under pressure: Different role of $d_{3z^2-r^2}$ orbital compared with $La_3Ni_2O_7$. Phys. Rev. B **109**(4), 045151 (2024) https://doi.org/10.1103/PhysRevB.109.045151

[27] Tian, Y.-H., Chen, Y., Wang, J.-M., He, R.-Q., Lu, Z.-Y.: Correlation effects and concomitant two-orbital $s_{\pm}$-wave superconductivity in $La_3Ni_2O_7$ under high pressure. Phys. Rev. B **109**(16), 165154 (2024) https://doi.org/10.1103/PhysRevB.109.165154

[28] Ryee, S., Witt, N., Wehling, T.O.: Quenched pair breaking by interlayer correlations as a key to superconductivity in $La_3Ni_2O_7$. Phys. Rev. Lett. **133**(9), 096002

(2024) https://doi.org/10.1103/PhysRevLett.133.096002

[29] Zhang, J.-X., Zhang, H.-K., You, Y.-Z., Weng, Z.-Y.: Strong pairing originated from an emergent Z_2 berry phase in $La_3Ni_2O_7$. Phys. Rev. Lett. **133**(12), 126501 (2024) https://doi.org/10.1103/PhysRevLett.133.126501

[30] Ni, X.-S., Ji, Y., He, L., Xie, T., Yao, D.-X., Wang, M., Cao, K.: Spin density wave in the bilayered nickelate $La_3Ni_2O_{7-\delta}$ at ambient pressure. npj Quantum Materials **10**(1), 1–9 (2025) https://doi.org/10.1038/s41535-025-00740-z

[31] Lu, C., Pan, Z., Yang, F., Wu, C.: Interlayer-coupling-driven high-temperature superconductivity in $La_3Ni_2O_7$ under pressure. Phys. Rev. Lett. **132**(14), 146002 (2024) https://doi.org/10.1103/PhysRevLett.132.146002

[32] Qu, X.-Z., Qu, D.-W., Chen, J., Wu, C., Yang, F., Li, W., Su, G.: Bilayer $t-J-J_\perp$ model and magnetically mediated pairing in the pressurized nickelate $La_3Ni_2O_7$. Phys. Rev. Lett. **132**(3), 036502 (2024) https://doi.org/10.1103/PhysRevLett.132.036502

[33] Yang, H., Oh, H., Zhang, Y.-H.: Strong pairing from a small fermi surface beyond weak coupling: Application to $La_3Ni_2O_7$. Phys. Rev. B **110**(10), 104517 (2024) https://doi.org/10.1103/PhysRevB.110.104517

[34] Fan, Z., Zhang, J.-F., Zhan, B., Lv, D., Jiang, X.-Y., Normand, B., Xiang, T.: Superconductivity in nickelate and cuprate superconductors with strong bilayer coupling. Phys. Rev. B **110**(2), 024514 (2024) https://doi.org/10.1103/PhysRevB.110.024514

[35] Sakakibara, H., Kitamine, N., Ochi, M., Kuroki, K.: Possible high T_c superconductivity in $La_3Ni_2O_7$ under high pressure through manifestation of a nearly half-filled bilayer hubbard model. Phys. Rev. Lett. **132**(10), 106002 (2024) https://doi.org/10.1103/PhysRevLett.132.106002

[36] Cao, Y., Yang, Y.-f.: Flat bands promoted by hund's rule coupling in the candidate double-layer high-temperature superconductor $La_3Ni_2O_7$ under high pressure. Phys. Rev. B **109**(8), 081105 (2024) https://doi.org/10.1103/PhysRevB.109.L081105

[37] Jiang, R., Hou, J., Fan, Z., Lang, Z.-J., Ku, W.: Pressure driven fractionalization of ionic spins results in cupratelike high-T_c superconductivity in $La_3Ni_2O_7$. Phys. Rev. Lett. **132**(12), 126503 (2024) https://doi.org/10.1103/PhysRevLett.132.126503

[38] Chen, X., Jiang, P., Li, J., Zhong, Z., Lu, Y.: Charge and spin instabilities in superconducting $La_3Ni_2O_7$. Phys. Rev. B **111**(1), 014515 (2025) https://doi.org/10.1103/PhysRevB.111.014515

[39] Yang, J., Sun, H., Hu, X., Xie, Y., Miao, T., Luo, H., Chen, H., Liang, B., Zhu, W., Qu, G., Chen, C.-Q., Huo, M., Huang, Y., Zhang, S., Zhang, F., Yang, F., Wang, Z., Peng, Q., Mao, H., Liu, G., Xu, Z., Qian, T., Yao, D.-X., Wang, M., Zhao, L., Zhou, X.J.: Orbital-dependent electron correlation in double-layer nickelate $La_3Ni_2O_7$. Nat Commun **15**(1), 4373 (2024) https://doi.org/10.1038/s41467-024-48701-7

[40] Zhang, Y., Su, D., Huang, Y., Shan, Z., Sun, H., Huo, M., Ye, K., Zhang, J., Yang, Z., Xu, Y., Su, Y., Li, R., Smidman, M., Wang, M., Jiao, L., Yuan, H.: High-temperature superconductivity with zero resistance and strange-metal behaviour in $La_3Ni_2O_{7-\delta}$. Nat. Phys. **20**, 1269–1273 (2024) https://doi.org/10.1038/s41567-024-02515-y

[41] Hou, J., Yang, P.-T., Liu, Z.-Y., Li, J.-Y., Shan, P.-F., Ma, L., Wang, G., Wang, N.-N., Guo, H.-Z., Sun, J.-P., Uwatoko, Y., Wang, M., Zhang, G.-M., Wang, B.-S., Cheng, J.-G.: Emergence of high-temperature superconducting phase in pressurized $La_3Ni_2O_7$ crystals. Chin. Phys. Lett. **40**(11), 117302 (2023) https://doi.org/10.1088/0256-307X/40/11/117302

[42] Fan, S., Luo, Z., Huo, M., Wang, Z., Li, H., Yang, H., Wang, M., Yao, D.-X., Wen, H.-H.: Tunneling spectra with gaplike features observed in nickelate $La_3Ni_2O_7$ at ambient pressure. Phys. Rev. B **110**, 134520 (2024) https://doi.org/10.1103/PhysRevB.110.134520

[43] Wang, G., Wang, N.N., Shen, X.L., Hou, J., Ma, L., Shi, L.F., Ren, Z.A., Gu, Y.D., Ma, H.M., Yang, P.T., Liu, Z.Y., Guo, H.Z., Sun, J.P., Zhang, G.M., Calder, S., Yan, J.-Q., Wang, B.S., Uwatoko, Y., Cheng, J.-G.: Pressure-Induced Superconductivity In Polycrystalline $La_3Ni_2O_{7-\delta}$. Phys. Rev. X **14**(1), 011040 (2024) https://doi.org/10.1103/PhysRevX.14.011040

[44] Liu, Z., Huo, M., Li, J., Li, Q., Liu, Y., Dai, Y., Zhou, X., Hao, J., Lu, Y., Wang, M., Wen, H.-H.: Electronic correlations and partial gap in the bilayer nickelate $La_3Ni_2O_7$. Nat Commun **15**(1), 7570 (2024) https://doi.org/10.1038/s41467-024-52001-5

[45] Li, Q., Zhang, Y.-J., Xiang, Z.-N., Zhang, Y., Zhu, X., Wen, H.-H.: Signature of Superconductivity in Pressurized $La_4Ni_3O_{10}$. Chin. Phys. Lett. **41**(1), 017401 (2024) https://doi.org/10.1088/0256-307X/41/1/017401

[46] Li, J., Peng, D., Ma, P., Zhang, H., Xing, Z., Huang, X., Huang, C., Huo, M., Hu, D., Dong, Z., Chen, X., Xie, T., Dong, H., Sun, H., Zeng, Q., Mao, H.-k., Wang, M.: Identification of the superconductivity in bilayer nickelate $La_3Ni_2O_7$ upon 100 GPa. arXiv (2025). https://doi.org/10.48550/arXiv.2404.11369

[47] Liu, Z., Huo, M., Li, J., Li, Q., Liu, Y., Dai, Y., Zhou, X., Hao, J., Lu, Y., Wang, M., *et al.*: Electronic correlations and partial gap in the bilayer nickelate $La_3Ni_2O_7$. Nat Commun **15**(1), 7570 (2024) https://doi.org/10.1038/

s41467-024-52001-5

[48] Ko, E.K., Yu, Y., Liu, Y., Bhatt, L., Li, J., Thampy, V., Kuo, C.-T., Wang, B.Y., Lee, Y., Lee, K., Lee, J.-S., Goodge, B.H., Muller, D.A., Hwang, H.Y.: Signatures of ambient pressure superconductivity in thin film $La_3Ni_2O_7$. Nature **638**(8052), 935–940 (2025) https://doi.org/10.1038/s41586-024-08525-3

[49] Zhou, G., Lv, W., Wang, H., Nie, Z., Chen, Y., Li, Y., Huang, H., Chen, W., Sun, Y., Xue, Q.-K., Chen, Z.: Ambient-pressure superconductivity onset above 40 K in $(La,Pr)_3Ni_2O_7$ films. Nature (2025) https://doi.org/10.1038/s41586-025-08755-z

[50] Liu, Y., Ko, E.K., Tarn, Y., Bhatt, L., Goodge, B.H., Muller, D.A., Raghu, S., Yu, Y., Hwang, H.Y.: Superconductivity and normal-state transport in compressively strained $La_2PrNi_2O_7$ thin films (2025). https://arxiv.org/abs/2501.08022

[51] Li, P., Zhou, G., Lv, W., Li, Y., Yue, C., Huang, H., Xu, L., Shen, J., Miao, Y., Song, W., Nie, Z., Chen, Y., Wang, H., Chen, W., Huang, Y., Chen, Z.-H., Qian, T., Lin, J., He, J., Sun, Y.-J., Chen, Z., Xue, Q.-K.: Angle-resolved photoemission spectroscopy of superconducting $La_{2.85}Pr_{0.15}Ni_2O_7/SrLaAlO_4$ heterostructures. National Science Review, 205 (2025) https://doi.org/10.1093/nsr/nwaf205

[52] Shen, J., Zhou, G., Miao, Y., Li, P., Ou, Z., Chen, Y., Wang, Z., Luan, R., Sun, H., Feng, Z., Yong, X., Li, Y., Xu, L., Lv, W., Nie, Z., Wang, H., Huang, H., Sun, Y.-J., Xue, Q.-K., He, J., Chen, Z.: Nodeless superconducting gap and electron-boson coupling in $(La,Pr,Sm)_3Ni_2O_7$ films (2025). https://arxiv.org/abs/2502.17831

[53] Yue, C., Miao, J.-J., Huang, H., Hua, Y., Li, P., Li, Y., Zhou, G., Lv, W., Yang, Q., Sun, H., Sun, Y.-J., Lin, J., Xue, Q.-K., Chen, Z., Chen, W.-Q.: Correlated electronic structures and unconventional superconductivity in bilayer nickelate heterostructures (2025). https://arxiv.org/abs/2501.06875

[54] Shao, Z.-Y., Liu, Y.-B., Liu, M., Yang, F.: Band Structure and Pairing Nature of $La_3Ni_2O_7$ Thin Film at Ambient Pressure (2025). https://arxiv.org/abs/2501.10409

[55] Bhatt, L., Jiang, A.Y., Ko, E.K., Schnitzer, N., Pan, G.A., Segedin, D.F., Liu, Y., Yu, Y., Zhao, Y.-F., Morales, E.A., Brooks, C.M., Botana, A.S., Hwang, H.Y., Mundy, J.A., Muller, D.A., Goodge, B.H.: Resolving Structural Origins for Superconductivity in Strain-Engineered $La_3Ni_2O_7$ Thin Films (2025). https://arxiv.org/abs/2501.08204

[56] Georges, A., Medici, L.d., Mravlje, J.: Strong correlations from hunds coupling. Annual Review of Condensed Matter Physics **4**(1), 137–178 (2013) https://doi.org/10.1146/annurev-conmatphys-020911-125045

[57] Bötzel, S., Lechermann, F., Gondolf, J., Eremin, I.M.: Theory of magnetic excitations in the multilayer nickelate superconductor $La_3Ni_2O_7$. Phys. Rev. B **109**,

180502 (2024) https://doi.org/10.1103/PhysRevB.109.L180502

[58] Kresse, G., Hafner, J.: Ab initio molecular dynamics for liquid metals. Phys. Rev. B **47**, 558–561 (1993) https://doi.org/10.1103/PhysRevB.47.558

[59] Kresse, G., Furthmüller, J.: Efficient iterative schemes for ab initio total-energy calculations using a plane-wave basis set. Phys. Rev. B **54**, 11169–11186 (1996) https://doi.org/10.1103/PhysRevB.54.11169

[60] Perdew, J.P., Burke, K., Ernzerhof, M.: Generalized gradient approximation made simple. Phys. Rev. Lett. **77**, 3865–3868 (1996) https://doi.org/10.1103/PhysRevLett.77.3865

[61] Böchl, P.E.: Projector augmented-wave method. Phys. Rev. B **50**, 17953–17979 (1994) https://doi.org/10.1103/PhysRevB.50.17953

[62] Pizzi, G., Vitale, V., Arita, R., Blügel, S., Freimuth, F., Géranton, G., Gibertini, M., Gresch, D., Johnson, C., Koretsune, T., Ibañez-Azpiroz, J., *et al.*: Wannier90 as a community code: new features and applications. J. Phys.: Condens. Matter **32**(16), 165902 (2020) https://doi.org/10.1088/1361-648x/ab51ff

[63] Marzari, N., Vanderbilt, D.: Maximally localized generalized wannier functions for composite energy bands. Phys. Rev. B **56**, 12847–12865 (1997) https://doi.org/10.1103/PhysRevB.56.12847

[64] Souza, I., Marzari, N., Vanderbilt, D.: Maximally localized wannier functions for entangled energy bands. Phys. Rev. B **65**, 035109 (2001) https://doi.org/10.1103/PhysRevB.65.035109

[65] Dudarev, S.L., Botton, G.A., Savrasov, S.Y., Humphreys, C.J., Sutton, A.P.: Electron-energy-loss spectra and the structural stability of nickel oxide: An LSDA+U study. Phys. Rev. B **57**, 1505–1509 (1998) https://doi.org/10.1103/PhysRevB.57.1505

[66] Georges, A., Medici, L.d., Mravlje, J.: Strong correlations from hund's coupling. Annual Review of Condensed Matter Physics **4**(Volume 4, 2013), 137–178 (2013) https://doi.org/10.1146/annurev-conmatphys-020911-125045

[67] Wang, B.Y., Zhong, Y., Abadi, S., Liu, Y., Yu, Y., Zhang, X., Wu, Y.-M., Wang, R., Li, J., Tarn, Y., Ko, E.K., Thampy, V., Hashimoto, M., Lu, D., Lee, Y.S., Devereaux, T.P., Jia, C., Hwang, H.Y., Shen, Z.-X.: Electronic structure of compressively strained thin film $La_2PrNi_2O_7$ (2025). https://arxiv.org/abs/2504.16372

[68] Zhao, Y.-F., Botana, A.S.: Electronic structure of Ruddlesden-Popper nickelates: Strain to mimic the effects of pressure. Phys. Rev. B **111**, 115154 (2025) https://doi.org/10.1103/PhysRevB.111.115154

[69] Bhatta, H.C.R.B., Zhang, X., Zhong, Y., Jia, C.: Structural and Electronic Evolution of Bilayer Nickelates Under Biaxial Strain (2025). https://arxiv.org/abs/2502.01624

[70] Geisler, B., Hamlin, J.J., Stewart, G.R., Hennig, R.G., Hirschfeld, P.J.: Fermi surface reconstruction and enhanced spin fluctuations in strained $La_3Ni_2O_7$ on $LaAlO_3(001)$ and $SrTiO_3(001)$ (2025). https://arxiv.org/abs/2411.14600

[71] Geisler, B., Hamlin, J.J., Stewart, G.R., Hennig, R.G., Hirschfeld, P.J.: Electronic reconstruction and interface engineering of emergent spin fluctuations in compressively strained $La_3Ni_2O_7$ on $SrLaAlO_4(001)$ (2025). https://arxiv.org/abs/2503.10902

Acknowledgements. We are grateful to Wéi Wú and Xiao-Hong Pan for useful discussions. Work at Sun Yat-Sen University was supported by the National Natural Science Foundation of China (Grants No. 12494591, No. 92165204), the National Key Research and Development Program of China (Grant No. 2022YFA1402802), Guangdong Provincial Key Laboratory of Magnetoelectric Physics and Devices (Grant No. 2022B1212010008), Research Center for Magnetoelectric Physics of Guangdong Province (Grant No. 2024B0303390001), Guangdong Provincial Quantum Science Strategic Initiative (Grant No. GDZX2401010), and Leading Talent Program of Guangdong Special Projects (201626003).

Author contributions. D.X.Y. and X.H. proposed and designed the project. X.H. and C.Q.C. contributed to DFT calculations. X.H. and D.X.Y. contributed to two-orbital models. W.Q. and D.X.Y. contributed to high-energy models. W.Q. and Z.L. contributed to spin susceptibility and discussion under the supervision of D.X.Y. All authors contributed to the interpretation of the results and wrote the paper.

Competing interests. The authors declare no competing interests.

Materials and Correspondence. Correspondence and requests for materials should be addressed to D.X.Y.